RSC Sustainability

ROYAL SOCIETY OF CHEMISTRY

PAPER

View Article Online
View Journal | View Issue

Cite this: *RSC Sustainability*, 2025, **3**, 1800

The importance of shape: flakes and spheres in recyclable conductive pastes for printed electronics†

David van Impelen, [a] Dominik Perius,[a] Lola González-García *[ab] and Tobias Kraus *[ac]

Silver microflakes and -spheres are common fillers for electrically conductive screen-printing pastes. Here, we report on the effects of filler shapes and sizes on conductivity, sintering, and recyclability. We printed pastes based on flakes and spheres, treated them at 110 °C to 300 °C, and evaluated the electrical conductivity of the resulting layers. The electrical conductivity of the layers treated at 110 °C was dominated by particle–particle contact resistances; flakes yielded layers that were five times more conductive than sphere-based layers due to differences in the particle–particle contact area. Increasing temperature led to a reduction of the resistivity of all layers through sintering. At 300 °C, prints based on spheres were 4 times more conductive than those from flakes. Tomography of the sintered structures showed that the difference was caused by a lower tortuosity factor for spheres. In a final study, we showed that silver flakes and spheres could be recycled after sintering and reused for a new generation of prints without losing electrical performance. The more porous structure of sintered flakes allowed for higher recycling yields compared to spheres. At 140 °C, 91.6% of the flakes and 69.7% of the spheres were recovered as reusable dispersions.

Received 18th November 2024
Accepted 11th February 2025

DOI: 10.1039/d4su00721b

rsc.li/rscsus

Sustainability spotlight

The conductive metal paste market for printed electronics is dominated by silver. Despite their excellent electrical performance, the ecological footprint of silver is large. We weakly sinter silver flakes and spheres at low temperatures and recycle and reuse the silver particles, significantly reducing the ecological footprint of the printed conductors. Flakes are more suited for recycling due to their porous nature after sintering, resulting in higher recycling yields than spheres. This work aims to reduce silver waste of printed electronics and therefore aligns with the following UN sustainable development goals (SDG): affordable and clean energy (SDG 7), responsible consumption and production (SDG 12), and climate action (SDG 13).

1 Introduction

Printing electronic devices and circuits with conductive paste or ink formulations makes effective use of conductive materials, enables low-temperature processing, and gives designers the possibility to use a large variety of substrates.[1,2] Conductive paste formulations for screen printing typically contain metal particles,[2] carbon materials,[3,4] or conductive polymers[5] in non-conductive polymer matrices. Silver particles dominate the market due to silver's high electrical conductivity, conductive oxide, and stability at high temperatures.[6,7] Heat treatments after printing remove solvent and sinter the particles, and a common challenge in paste development is to reach a high conductivity at low or moderate temperatures and after short times.

Silver nanoparticles can rapidly fuse at low temperatures.[8] They have large specific surfaces that are strongly curved, and the diffusion paths between particles are short. Treatments below 200 °C thus result in highly conductive prints with a resistivity ranging from 3.45 μΩ cm to 8.0 μΩ cm. However, nanoparticles are expensive and prone to agglomeration. Stabilized nanoparticles carry a relatively large fraction of stabilizing organics that form pores and reduce conductivity.[1,8]

Silver microparticles are more readily available, contain lower amounts of organics, and are cheaper than nanoparticles. They are often used as conductive fillers for metal-based screen printing pastes. Experimental studies have shown that silver microparticles can be sintered at temperatures below 200 °C to obtain resistivities down to 8.33 μΩ cm.[9–12] The observed sintering times are much shorter than predicted diffusion-based

[a]*INM – Leibniz-Institute for New Materials, Campus D2 2, 66123 Saarbrücken, Germany. E-mail: lola.gonzalez-garcia@leibniz-inm.de; tobias.kraus@leibniz-inm.de*
[b]*Saarland University, Department of Materials Science and Engineering, Campus D2 2, 66123 Saarbrücken, Germany*
[c]*Saarland University, Colloid and Interface Chemistry, Campus D2 2, 66123 Saarbrücken, Germany*

† Electronic supplementary information (ESI) available. See DOI: https://doi.org/10.1039/d4su00721b

sintering models.[13] D. van Impelen *et al.* report that silver was not transported among microspheres with classical surface or bulk diffusion processes, but involved the creation of mobile ionic silver that rapidly diffused and precipitated to form necks. This mechanism was aided by residual organic molecules so that the onset temperature depended on the production method of the particles.[12] Surfactant-containing precipitated silver particles started sintering at 140 °C, compared to 275 °C for surfactant-free atomized silver particles.

Silver microflakes are a common alternative filler.[10,14–20] Prints based on flakes can reach low resistivities down to 284 μΩ cm upon drying and without sintering, which has been attributed to the high particle–particle interface area caused by the alignment of flakes.[21] Some groups reported that micro flakes can be sintered at lower temperatures than microspheres[14,15,22] due to microstrains in flakes.[22] The release of this microstrain resulted in the formation of nanoparticles, which aided the sintering.

Silver is an expensive material and its production has a significant environmental impact. A life cycle analysis by Naji *et al.* identified the conductive metal inks as the largest environmental impact factor of printed electronic.[23] Recycling of metal powders can significantly reduce this impact. Kang *et al.* designed a recyclable gold nanoparticle ink for inkjet printing.[24] The printed ink could be separated from the substrate and the particles were redispersed by sonication to form a recovered ink formulation. Kwon *et al.* printed conductors based on silver micro flakes and were able to recycle the silver particles.[25] They formulated new pastes from the recovered silver particles and the recycled printed conductors had similar electrical performances. None of these inks were sintered, however, and their conductivities were orders of magnitude above that of silver. D. van Impelen *et al.* studied weakly sintered silver microparticle structures and found that weak sinter necks could be broken to recover printable silver particles.[12] They reported a trade-off between reducing the resistance of the prints through sintering and the ease of recycling the particles. We are not aware of any reports on the recycling of prints based on silver micro flakes.

This manuscript directly compares the conductivities and the recyclabilities of silver microspheres and -flakes in printed layers after heat treatments at 110 °C to 300 °C. We provide an explanation for the increased conductivity observed for flakes treated at lower temperatures and spheres treated at higher temperatures and show that flakes have a higher recycling efficiency. The resulting data enables a rational choice of particle geometry and sintering temperatures depending on the desired application. To our knowledge, we are the first to compare the electrical conductivity and recyclability of printed silver flakes and spheres sintered at low and high temperatures.

2 Materials and methods

2.1 Metal powders

Precipitated silver microspheres with average diameters of 1 and 1.5 μm (S14024-NM1 and S14010-NM1 Ag powder, Ames Goldsmith, United Kingdom) and precipitated micro flakes with average equivalent diameters of 2.8 and 3.2 μm (SF65 and SF91 Ag powder, Ames Goldsmith, United Kingdom) were purchased. The volume–equivalent sphere diameters of the flakes reported here were obtained from laser diffraction.

2.2 Printing and preparation of paste

Pastes were prepared by mixing the particles with Ethylene Glycol (EG, anhydrous 98%, Sigma-Aldrich) at a weight ratio of Ag : EG of 5 : 1 for flakes and 10 : 1 for spheres. A bladeless mixer (SpeedMixer DAC 150.3 SP, Hauschild, Germany) operated at 2350 rpm for 3 min ensured the formation of homogeneous, highly viscous pastes. The pastes were used to screen-print rectangles of 1 × 3 cm^2 with a manual screen printer using a mesh of 100 polyester threads per centimeter on microscopy glass slides (VWR, ground edge frosted, Germany). The thickness of the printed layers was determined with a 3D confocal microscope MarSurf CM explorer (Mahr, Germany) by averaging three measurements on three samples. Prints containing 2.8 and 3.2 μm flakes had average thicknesses of 18.9 and 18.2 μm, prints containing 1 and 1.5 μm spheres had 17.5 and 21 μm. Prints used for the experiments described in the section 'Sintering of flakes and spheres at different temperatures' were placed in a preheated oven (Thermoscientific VACUtherm, Germany) for 30 min. Prints used in experiments in Section 3.2 were placed on a preheated hotplate with a closed lid (PZ28-3TD, Präzitherm, Germany) coupled to a PID controller (PR5-3T, Präzitherm, Germany) for 30 min. All reported resistance values in this manuscript are an average of at least three samples.

2.3 Characterization methods

The weight fraction of surfactants on the particle surface was quantified with Thermogravimetric Analysis (TGA, PerkinElmer TGA 8000, Germany). 20 mg powder was heated in N_2 from 30 °C to 400 °C at 10 °C min^{-1}, then to 900 °C at 30 °C min^{-1}.

A four-point probe measurement set-up with a 2450 Sourcemeter (Keithley Instruments, Ohio, USA) using four in-line conical gold pins (GKS-069 201051 A 0700, Ingun, Germany) with a pin-to-pin distance of 1 mm was used to measure the resistance of the printed samples. The mass-normalized sheet resistance was determined, as introduced in previous work,[12]

$$R_{m/sh} = m \times R_{sh}, \quad (1)$$

where m is the printed metal mass and R_{sh} the sheet resistance of the printed sample. The mass-normalized sheet resistance is closely related to the well-established sheet resistance, but it is a material property that considers that effect of material use, a key advantage in work on resource efficiency.

A dual beam electron microscope (FEI Versa 3D Dualbeam) was employed for focused ion beam scanning electron microscopy (FIB-SEM) tomography. Software (Autoslice and View G3, Thermo Scientific, USA) was used to control the microscope and automatically remove 350 slices of width 90 nm at an ion current of 5 nA and 30 kV. After every slice, a tilt-corrected secondary electron (SE) image (1536 × 1024 pixel, 90 nm pixel

size) was recorded at a magnification of 1500 and a dwell-time of 1 μs. The SE images were reconstructed using the AVIZO software (Version 2021, Thermo Scientific): the data processing included image stack alignment, shearing, and cropping before edge-preserving non-local means filtering yielded the final, 3D-reconstructed image stack. The stacks were subsequently segmented using manual grayscale histogram thresholding. For a detailed description and a review of FIB-SEM tomography, we refer the reader to the work of Holzer and Cantoni.[26] The silver phase provided good contrast against the pore space. This enabled us to set the threshold at the minimum between the two present maxima of the two-phase (pores and silver) gray-scale histogram. Reconstructed volumes of size 46.8 μm × 15.6 μm × 15.6 μm were cropped to obtain three isotropic, binary cubes of size $(15.6\ \mu m)^3$, where the silver phase voxels had a value 1 and the pore space 0. Each cube was exported to a single .tif file and used as input for the MATLAB code Tau-factor,[27] which simulated Fickian diffusion on the silver phase voxels. The diffusional tortuosity (tortuosity factors) was calculated by simulating the diffusional flux against a concentration gradient for the silver phase and a homogeneous representative volume element (REV)[28] in every direction and dividing their resulting fluxes to yield the tortuosity factors $\tau_{d,x}$, $\tau_{d,y}$ and $\tau_{d,z}$. The individual directions were summarized in $\tau_{d,3D}$ as the root-mean-square of the individual directions. In total three cubes for each sample were computed to obtain the mean $\overline{\tau_{g,3D}}$. Geometrical tortuosity was calculated using the MATLAB code "Tort3D" from Cecen *et al.*[29] This code calculates the distribution of geometrical tortuosities from the binary volume in the *z*-direction only. We rotated the cubes twice to obtain the distributions for all spatial directions. The root-mean-squares of the average $\tau_{g,x}$, $\tau_{g,y}$ and $\tau_{g,z}$ were calculated for each cube to obtain the three-dimensional equivalent $\tau_{g,3D}$ of the geometrical tortuosity, and again from three cubes the mean $\overline{\tau_{g,3D}}$ was used to compare flakes and spheres.

3 Results and discussion

3.1 Sintering of flakes and spheres at different temperatures

We prepared pastes containing silver flakes and spheres. Silver flakes (Ag–F) had average diameters (of the volume–equivalent spheres) of 2.8 and 3.2 μm and the spheres (Ag–S) of 1 and 1.5 μm. Spheres had monomodal size distributions, while flakes had bimodal size distributions with a peak at 1 μm and a peak between 3 and 4 μm. Flakes had higher specific surface areas: 1.11 and 0.71 $m^2\ g^{-1}$ for 2.8 and 3.2 μm Ag–F compared to 0.37 and 0.26 $m^2\ g^{-1}$ for 1 and 1.5 μm Ag–S.

The spheres were produced by chemical precipitation and contained 0.41 and 0.33 wt% of surfactants. The flakes were made by mechanical milling of precipitated spheres and contained 0.5 and 0.4 wt% of surfactants. The pastes were screen printed on glass and treated in the oven at 110 °C to 300 °C for 30 min. We used the mass-normalized sheet resistances ($R_{m/sh}$) introduced in previous work[12] to electrically characterize the prints (see Section 2.3). In addition, a comparison with prints containing 1.8 μm-sized flakes can be found in Fig. S1 of the ESI.†

Fig. 1 illustrates the decreasing mass-normalized sheet resistances after thermal annealing for all prints. At 110 °C, the prints containing silver flakes reached $R_{m/sh} \approx 3.0\ m\Omega\ sq^{-1}\ g^{-1}$, considerably below that of spheres at $R_{m/sh} \approx 14.9\ m\Omega\ sq^{-1}\ g^{-1}$. Both spheres and flakes largely retained their original sizes and shapes (see Fig. S2 in the ESI†), and SEM imaging did not reveal the formation of sinter necks (see Fig. 1C and D).

Literature agrees that the resistance of dried metal particle prints is dominated by the particle–particle contact resistances.[30–32] They are caused by the constriction resistances due to the small particle–particle contacts and tunneling resistances due to insulating interlayers.[32] We propose that layers treated at 110 °C are still dominated by contact resistances. Flakes have larger overall particle–particle contact areas,

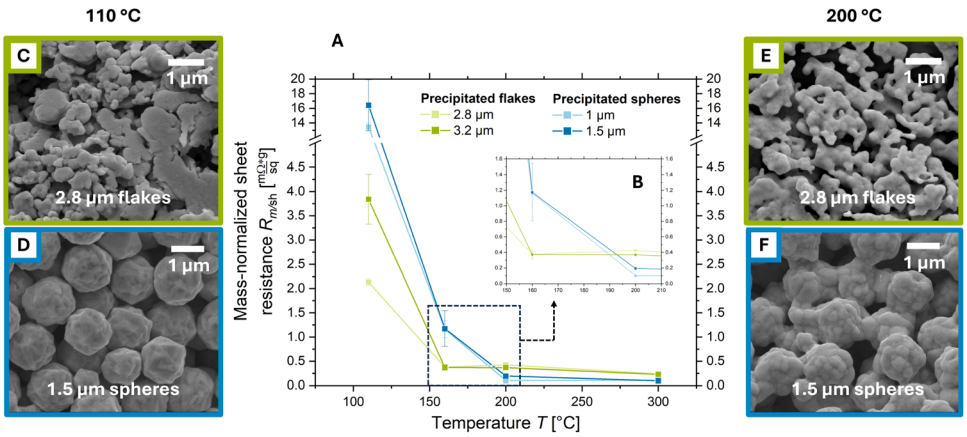

Fig. 1 Electrical conductivities and microstructures of prints containing silver flakes and spheres after thermal annealing for 30 min. (A) Mass-normalized sheet resistances $R_{m/sh}$ as a function of temperature T for prints containing 2.8 or 3.2 μm flakes (green lines), and 1 or 1.5 μm spheres (blue lines). (B) Inset: resistance changes at 150 °C to 200 °C, where sphere become more conductive than flake prints. (C) Top-view scanning electron micrographs of prints containing 2.8 μm flakes and (D) 1.5 μm spheres treated at 110 °C. (E and F) The same for flake and sphere prints after treatment at 200 °C.

which (at comparable particle sizes and surface states) reduces the overall contact resistances and thus, $R_{m/sh}$.[18]

Annealing at higher temperatures changed the picture. For silver flakes, $R_{m/sh}$ decreased with increasing temperature and reached $R_{m/sh} \approx 0.4$ mΩ sq^{-1} g^{-1} at 160 and 200 °C and $R_{m/sh} \approx 0.2$ mΩ sq^{-1} g^{-1} at 300 °C. Layers made from silver spheres became more conductive at elevated temperatures: their resistances reached $R_{m/sh} \approx 1.2$ mΩ sq^{-1} g^{-1} at 160 °C, but dropped to $R_{m/sh} \approx 0.1$ mΩ sq^{-1} g^{-1} at 200 and 300 °C. This is approximately twice that of bulk silver ($R_{m/sh,Ag} = 0.05$ mΩ sq^{-1} g^{-1}).

Fig. 1E and F illustrate the sinter necks that formed at 200 °C for flakes and spheres, respectively. After the formation of such necks, conducting electrons no longer need to tunnel from particle to particle, since the particles are now interconnected. The contact resistances decrease and become dominated by the constriction resistance, which strongly depends on neck size.[32,33]

We propose that the necks are responsible for the drop in $R_{m/sh}$ that we observed for both flakes and spheres above 110 °C. At first, the tunneling contacts are converted into sinter necks, leading to a sharp decrease in $R_{m/sh}$. The growth of initially formed necks more slowly reduces $R_{m/sh}$ through the reduction of the restriction resistance.[32] The drop in $R_{m/sh}$ strongly slowed down above 160 °C for flakes and above 200 °C for spheres. At 300 °C, large necks had formed and converted the printed structures into a porous metal (see Fig. S3 of the ESI†).

The $R_{m/sh}$ of the porous metal formed at 300 °C was 4 times that of bulk polycrystalline silver[34] for flakes and 2 times that for spheres. Multiple studies have shown that nanocrystalline metals have higher resistivities than polycrystalline metals due to the large numbers of grain boundaries.[35–37] We measured the grain size of the porous metal formed from silver flakes and spheres sintered at 300 °C using X-ray diffraction (XRD) and found sizes of 46 and 48 nm, respectively (see Fig. S4 of the ESI†). This difference is too small to explain the bulk conductivity differences: Qin *et al.* measured a resistivity of 2.4 μΩ cm for nanocrystalline silver with an average grain size of 25 nm and 1.6 μΩ cm for micron-sized grains.[35] We thus attribute the increased $R_{m/sh}$ to the remaining porosity.

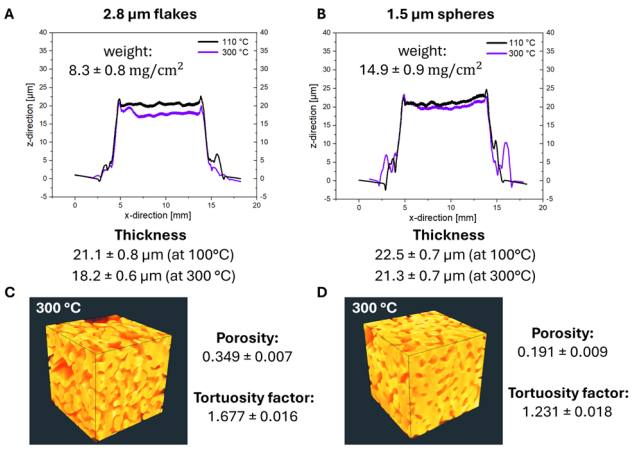

Fig. 2 Structures of sintered prints of flakes and spheres. Surface profiles of prints treated at 110 and 300 °C containing (A) 2.8 μm flakes and (B) 1.5 μm spheres from confocal microscopy. 3D reconstructions from FIB-SEM tomography of (C) prints based on 2.8 μm flakes treated at 300 °C and (D) prints based on 1.5 μm spheres treated at 300 °C.

The thicknesses and weights of prints containing 2.8μm-sized flakes (Fig. 2A) and 1.5 μm-sized spheres (Fig. 2B) treated at 110 and 300 °C indicate minimal shrinkage for both, in agreement with initial stage sintering.[33] Interestingly, the average thicknesses of flake- and spherical-based prints were comparable, but the average weight per area of the sphere-based prints was almost twice that of flake-based prints. This suggests a higher porosity of flake-based prints.

We determined the porosities of sintered prints treated at 300 °C by cutting microscopic volumes of size 46.8 μm × 15.6 μm × 15.6 μm with a focused ion beam from the samples, removing slices from it and recording 175 electron micrographs (Fig. 2, see Materials and methods). Porosities and the geometrical and diffusional tortuosities of the silver phase were then calculated for three subvolumes as described in the Methods section and averaged.

The average porosity of flake-based prints was found to be 0.349 compared to only 0.191 of sphere-based prints. One might expect that flakes can pack efficiently in a tile-like fashion, but Yoshinaga *et al.* already noticed that metal microspheres pack more densely than flakes of comparable sizes.[38] They studied packing in compressed powder electrodes; we propose that screen-printing of viscous pastes also leads to porous flake arrangements.

The higher porosity of the sintered flake structures explains the difference in $R_{m/sh}$. Random porosity causes constrictions and extends the lengths of conductive paths, increasing macroscopic electrical resistance. The geometrical tortuosity of our printed structures can be quantified using the geometrical tortuosity

$$\tau_g = \frac{L_g}{L}, \quad (2)$$

where L_g is the length of the transport path and L the Euclidean distance between the start- and endpoint of the path.[39] Large τ_g imply longer transport paths that can indicate larger overall resistances, but τ_g does not describe constrictions. The diffusional tortuosity has been defined to consider the effect of passages with small cross-sections:

$$\tau_d = \frac{D \cdot \varepsilon}{D_{eff}}, \quad (3)$$

where D_{eff} is the diffusivity through a porous volume with impenetrable walls, D is the intrinsic diffusivity, and ε the porosity. τ can be used as a measure of electrical conductivity because electron transport in a potential gradient follows the same functional form as diffusion in a concentration gradient.[40]

We calculated geometrical and diffusional tortuosity factors of our samples from their reconstructed geometries using the open-source MATLAB codes "Tort3D"[29] and "TauFactor",[27] respectively. Voxelized binary data from segmented 3D reconstructions of the silver phase of the prints were used as input. The average τ was 1.164 ± 0.001 for the sintered flakes,

compared to 1.069 ± 0.003 for the sintered spheres. The differences are small and both values close to 1, indicating that the different porosities did not perceptibly increase the average path length of conducting electrons.

The diffusional tortuosities τ_d, however, were clearly different at 1.677 ± 0.018 for sintered flakes and 1.231 ± 0.016 for sintered spheres. The conductive paths in flake-based metal layers had more constrictions that locally increased the electrical resistance. They explain the higher $R_{m/sh}$ of layers made by sintering flakes even when the silver content was identical to that of spheres. In summary, the flake prints electrically outperformed sphere prints after a treatment at 110 °C for 30 min. We propose that this difference stems from larger particle–particle contact areas between the flakes that reduce $R_{m/sh}$. Increasing temperature led to a cross-over at 200 °C because spheres yielded denser layers that provided conductive paths with less geometrical constrictions.

3.2 Recycling of flakes and spheres

The different contact geometries suggest that the recyclability of weakly sintered films differs for spheres and flakes. To test this, pastes containing 2.8 μm flakes and 1.5 μm spheres were printed, treated at different temperatures, recycled, and used for new prints. The results are shown in Fig. 3.

Fig. 3A shows the circular process of printing and recycling. Pastes containing spheres or flakes were printed and treated at 120, 140, and 160 °C. The resistances of the prints are given in Fig. 3B as 'initial'. The printed metal was then mechanically removed from the substrate to obtain "recovered powder" (see Fig. 3A). The recovered powder contained individual particles and sintered aggregates. The size of sinter necks increased with increasing treatment temperature, leading to more strongly sintered aggregates in the recovered powder (see Fig. S5 of the ESI†). To avoid clogging during screen-printing, we fragmented aggregates by probe sonication in isopropanol (IPA). The sonicated suspension was kept at rest for 2 min so that it formed two phases: sedimented powder at the bottom and dispersion in the supernatant (see Fig. 3A). The sediment contained large aggregates, the dispersion smaller aggregates or individual particles. The supernatant was decanted, centrifuged, and dried to obtain the recycled powder. The sediment that could not be dispersed was removed and considered as loss. The recycling yields indicated in Fig. 3B were determined by dividing the weight of recycled powder by the total weight of the recovered powder. The recycled powder was then reused to create a new paste, printed, and treated at the same temperature as the initial prints. $R_{m/sh}$ of the recycled prints are shown in Fig. 3B.

At 120 °C, 99.6% of the flakes and 94.2% of the spheres were recycled. At 140 °C, 91.6% of the flakes were recycled but only 69.7% of the spheres; at 160 °C, recycling yields were 44.7% for flakes and 33.2% for spheres.

The results are consistent with the evolution of sinter necks. No necks had formed at 120 °C (see Fig. S5 of the ESI†), minimizing the loss fraction and maximizing the recycling percentage both of flakes and spheres. The situation changed at 140 °C. Flakes and spheres formed visible sinter necks (see Fig. S5 of the ESI†) that yielded sintered aggregates in the recovered powder. Consequently, the loss fraction increased and the recycling yield decreased. The yield decreased more rapidly with temperature for spheres than for flakes. Printed flakes were 1.8 times more porous than printed spheres. We propose that the higher porosity made the flake layers mechanically weaker and eased the breakup of aggregates in the recovered powder. The improved redispersibility reduced the loss fraction and aided recycling (see Fig. 4). This is consistent with the results of Wakamoto *et al.*, who compared the

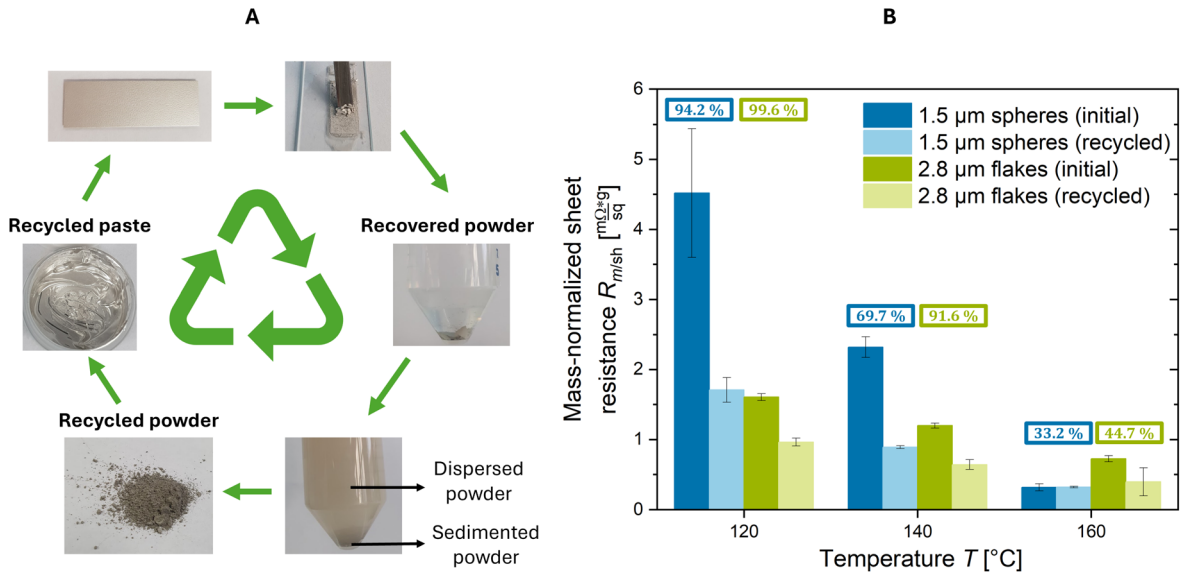

Fig. 3 The recycling of sintered prints of flakes and spheres followed the process shown in (A). Weight-normalized sheet resistances $R_{m/sh}$ of prints of new ('initial') and recycled particles are shown in (B) as a function of sintering temperature T for 1.5 μm spheres (blue) and 2.8 μm flakes (green) treated for 30 min. The weight fractions indicate how much powder was recycled from the initial prints.

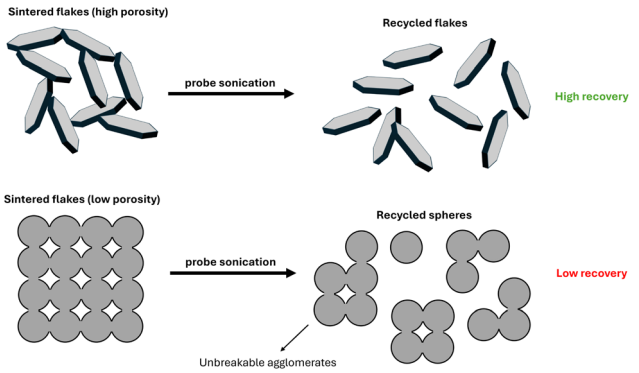

Fig. 4 Aggregates of sintered flakes were mechanically weaker and more easily dispersed by probe sonication. Aggregates of sintered spheres were stronger, increasing the powder loss fraction.

mechanical properties of sintered silver films at porosities of 5, 6, 14, and 25%.[41] They used tensile testing to show that their ultimate tensile strength decreased with porosity, while brittle fracture occurred at lower strains.

The sinter necks at 160 °C were larger, making the aggregates more difficult to break (see Fig. S5 of the ESI†). Consequently, a larger amount ended up in the loss fraction, leading to lower recycling yields both for flakes and spheres (see Fig. 4B).

The $R_{m/sh}$ of the initial prints decreases with increasing temperature for spheres and flakes, consistent with the formation of sinter necks. Initial prints consistently had greater $R_{m/sh}$ than recycled prints. We found small aggregates with visible sinter necks in electron micrographs of the recycled powders (Fig. S6 of the ESI†). We propose that they are small enough to fit through the screen-printing mesh, which has a mesh opening size of 60 μm, get embedded in the recycled prints, and lower $R_{m/sh}$ through reducing the sum of particle–particle contact resistances.

4 Conclusion and discussion: flakes or spheres?

We compared microscale silver flakes and spheres in metal-based printed conductors. Conductivities, sintering mechanisms, and recyclabilities of prints with different particles at the same silver mass loading per unit area were compared.

Conductive prints were obtained after 30 min at 110 °C for both flake- and sphere-based prints. Neither flakes nor spheres sintered under these conditions, but tunnel barriers were removed. Flakes clearly outperformed spheres in conductivity, they had only a quarter of the mass-normalized sheet resistance $R_{m/sh}$ of spheres. We attribute this advantage to the larger overall particle–particle contact area of flakes in prints.

Temperatures above 110 °C reduced $R_{m/sh}$ through the formation of sinter necks. The conductivity of sphere prints exceeded that of flake prints when sintering at 200 °C and above. $R_{m/sh}$ of spheres dropped to half of that of flakes and remained at this level when increasing temperature. Layers of sintered spheres were less porous and had lower tortuosity factors than flake-based prints, explaining this difference.

The recycling of printed flakes yielded larger yields than that of spheres. The higher porosity of sintered flake layers aided the mechanical breakup of aggregates and minimized the sedimented loss fraction. At 140 °C, 91.6% of the flakes but only 69.7% of the spheres were recycled.

Overall, silver flakes are more suited for low thermal budget, highly conductive, and recyclable printed conductors. Silver spheres enable reaching the lowest possible resistivity. Sintering the spheres at 200 °C for 30 min resulted in a $R_{m/sh}$ of only twice that of bulk silver.

Data availability

The data that support the findings of this study are available from the corresponding author, Tobias Kraus, upon reasonable request.

Author contributions

David van Impelen wrote the original draft of the manuscript and performed the majority of the experiments. Dominik Perius performed FIB-SEM tomography, made the 3D reconstructions, and wrote the section on tortuosities and 3D reconstructions. All authors took part in the conceptualization, reviewing, and editing of the manuscript. Tobias Kraus and Lola González-García were leading the supervision. Tobias Kraus was responsible for the funding acquisition and resources.

Conflicts of interest

There are no conflicts of interest to declare.

Acknowledgements

We acknowledge Albenc Nexha for the X-ray diffraction analyses. This work was supported by the German Federal Foundation for the Environment (DBU). We thank Jochen Wahl (CEO of GSB Wahl GmbH) for his contributions to discussions on low-impact conductive pastes.

Notes and references

1 S. Wünscher, R. Abbel, J. Perelaer and U. S. Schubert, *J. Mater. Chem. C*, 2014, **2**, 10232–10261.
2 C. Cano-Raya, Z. Z. Denchev, S. F. Cruz and J. C. Viana, *Appl. Mater. Today*, 2019, **15**, 416–430.
3 B. Nguyen and H. Nguyen Van, *Adv. Nat. Sci.:Nanosci. Nanotechnol.*, 2016, **7**, 023002.
4 Q. Huang and Y. Zhu, *Adv. Mater. Technol.*, 2019, **4**, 1800546.
5 W. Lövenich, *Polym. Sci., Ser. C*, 2014, **56**, 135–143.
6 S. Paknejad, G. Dumas, G. West, G. Lewis and S. Mannan, *J. Alloys Compd.*, 2014, **617**, 994–1001.
7 K. Rajan, I. Roppolo, A. Chiappone, S. Bocchini, D. Perrone and A. Chiolerio, *Nanotechnol., Sci. Appl.*, 2016, **9**, 1–13.

8 L. Mo, Z. Guo, L. Yang, Q. Zhang, Y. Fang, Z. Xin, Z. Chen, K. Hu, L. Han and L. Li, *Int. J. Mol. Sci.*, 2019, **20**, 2124.
9 Z. Guo, J. Lang, H. Zhang, C. Yang, S. Lin and H. Wu, *Adv. Mater. Interfaces*, 2022, **9**(26), 2196–7350.
10 H. Zhan, J. Guo, X. Yang, B. Guo, W. Liu, H. Shen, X. Wang, W. Tang and F. Chen, *J. Mater. Sci.: Mater. Electron.*, 2019, **30**, 21343–21354.
11 Y. Jeyun, Z. Hao, L. Cai-Fu and S. Katsuaki, *J. Mater. Sci.: Mater. Electron.*, 2019, **30**, 18080–18087.
12 D. van Impelen, L. González-García and T. Kraus, *Adv. Electron. Mater.*, 2024, 2400533.
13 X. Wang and L. Benabou, *Mech. Adv. Mater. Struct.*, 2022, **29**, 1601–1613.
14 C. Chen and K. Suganuma, *Mater. Des.*, 2018, **162**, 311–321.
15 C. Chen, J. Yeom, C. Choe, G. Liu, Y. Gao, Z. Zhang, B. Zhang, D. Kim and K. Suganuma, *J. Mater. Sci.*, 2019, **54**, 1247–1256.
16 C. Chen, Z. Zhang, B. Zhang and K. Suganuma, *J. Mater. Sci.:Mater. Electron.*, 2020, **31**, 1247–1256.
17 W. Li, Y. Li, Y. Wang, Y. Liu, C. Chen, J. Zhang and H. Yan, *J. Mater. Process. Technol.*, 2023, **322**, 118207.
18 W. Li, X. Xu, W. Li, Y. Zhao and M. Chen, *J. Mater. Sci.*, 2018, **53**, 6424–6432.
19 S.-C. Fu, M. Zhao, H. Shan and Y. Li, *Mater. Lett.*, 2018, **226**, 26–29.
20 H. Zhang, C. Chen, J. Jiu and K. Suganuma, Solvent effect on pressureless and low-temperature sintering of Ag paste for die-attachment in high-power devices, *2017 18th International Conference on Electronic Packaging Technology*, IEEE, 2017, pp. 624–627.
21 T. Nakanishi, K. Yamagishi, E. Iwase, H. Iwata, S. Takeoka and T. Fujie, *Appl. Phys. Express*, 2019, **12**, 7.
22 Y. Jeyun, N. Shijo, C. Chuantong, S. Tohru, Z. Hao, C. Chanyang, L. Cai-Fu and S. Katsuaki, *Appl. Phys. Lett.*, 2019, **114**, 253103.
23 M. Naji, M. Valimaki, L. Hakola, K. Eiroma, K. Immonen, M. Abdulkareem and M. Horttanainen, *Flexible Printed Electron.*, 2023, **8**, 025015.
24 D. Kang, Y. Jüttke, L. Gonzalez-Garcia, A. Escudero, M. Haft and T. Kraus, *Small*, 2020, **16**, 2000928.
25 J. Kwon, C. DelRe, P. Kang, A. Hall, D. Arnold, I. Jayapurna, L. Ma, M. Michalek, R. Ritchie and T. Xu, *Adv. Mater.*, 2022, **34**, 2202177.
26 L. Holzer and M. Cantoni, *Nanofabrication Using Focused Ion and Electron Beams: Principles and Applications*, 2012, 559201222, pp. 410–435.
27 S. Cooper, A. Bertei, P. Shearing, J. Kilner and N. Brandon, *SoftwareX*, 2016, **5**, 203–210.
28 J. Fu, H. R. Thomas and C. Li, *Earth-Sci. Rev.*, 2021, **212**, 103439.
29 A. Cecen, E. Wargo, A. Hanna, D. Turner, S. Kalidindi and E. Kumbur, *J. Electrochem. Soc.*, 2012, **159**, B299.
30 S. Shenogin, L. Ferguson and A. K. Roy, *Polymer*, 2020, **198**, 122502.
31 Y. Mamunya, H. Zois, L. Apekis and E. Lebedev, *Powder Technol.*, 2004, **140**, 49–55.
32 E. Sancaktar and Y. Wei, *J. Adhes. Sci. Technol.*, 1996, **10**, 1221–1235.
33 R. M. German, *Sintering: from Empirical Observations to Scientific Principles*, Butterworth-Heinemann, Boston, 2014.
34 D. Lide, *CRC Handbook of Chemistry and Physics*, 2007.
35 X. Y. Qin, W. Zhang, L. D. Zhang, L. D. Jiang, X. J. Liu and D. Jin, *Phys. Rev. B:Condens. Matter Mater. Phys.*, 1997, **56**, 10596–10604.
36 I. Bakonyi, *Eur. Phys. J. Plus*, 2021, **136**, 410.
37 C. Su and X. Su, *Comput. Mater. Sci.*, 2015, **108**, 62–65.
38 H. Yoshinaga, Y. Arami, O. Kajita and T. Sakai, *J. Alloys Compd.*, 2002, **330**, 846–850.
39 P. Adler, C. Jacquin and J. Quiblier, *Int. J. Multiphase Flow*, 1990, **16**, 691–712.
40 T.-T. Nguyen, A. Demortière, B. Fleutot, B. Delobel, C. Delacourt and S. J. Cooper, *npj Comput. Mater.*, 2020, **6**, 123.
41 K. Wakamoto, Y. Mochizuki, T. Otsuka, K. Nakahara and T. Namazu, *Jpn. J. Appl. Phys.*, 2019, **58**, SDDL08.